

# Biomechanical 3-D Finite Element Modeling of the Human Breast Using MRI Data

Abbas Samani\*, Jonathan Bishop, Martin J. Yaffe, and Donald B. Plewes

**Abstract**—Breast tissue deformation modeling has recently gained considerable interest in various medical applications. A biomechanical model of the breast is presented using a finite element (FE) formulation. Emphasis is given to the modeling of breast tissue deformation which takes place in breast imaging procedures. The first step in implementing the FE modeling (FEM) procedure is mesh generation. For objects with irregular and complex geometries such as the breast, this step is one of the most difficult and tedious tasks. For FE mesh generation, two automated methods are presented which process MRI breast images to create a patient-specific mesh. The main components of the breast are adipose, fibroglandular and skin tissues. For modeling the adipose and fibroglandular tissues, we used eight noded hexahedral elements with hyperelastic properties, while for the skin, we chose four noded hyperelastic membrane elements. For model validation, an MR image of an agarose phantom was acquired and corresponding FE meshes were created. Based on assigned elasticity parameters, a numerical experiment was performed using the FE meshes, and good results were obtained. The model was also applied to a breast image registration problem of a volunteer's breast. Although qualitatively reasonable, further work is required to validate the results quantitatively.

**Index Terms**—Breast, finite element analysis, image registration, mesh generation, MRI.

## I. INTRODUCTION

**P**REDICTING breast tissue deformation is of great significance in several medical applications such as surgery, biopsy and imaging. In breast surgery, surgeons are often concerned with a specific portion of the breast, e.g., tumor, which must be located accurately beforehand. Locating the portion of interest is done using imaging techniques which are done under tissue configuration of compression or body position that is often entirely different from that of surgery. In this case, nonrigid image registration is required to locate the portion of interest in the new configuration. In breast biopsy, the biopsy

needle causes the breast tissue to deform which may lead the tumor to displace. This deformation renders the guiding images less accurate unless the displacements are determined and needle aiming is corrected accordingly. In multimodality imaging of the breast, images of different modalities are often obtained under different tissue configurations of compression, orientation, or body position. In this case, determining the tissue deformation is essential for facilitating data fusion [1]. FEM has been widely used in modeling biological tissues such as bone [2]–[4] and myocardium [5], and recently in modeling brain deformation [6]–[8]. This work is aimed at using FEM in modeling breast tissue deformation.

For a FE model to be satisfactory in predicting deformation and other relevant parameters, in addition to using accurate elasticity parameters and boundary conditions, a reasonably accurate FE geometry model is essential. As the breast is composed of soft tissues, large deformation is usually created while undergoing medical procedures. In this paper, large deformation is considered in the FE formulation, and soft tissues are modeled as incompressible hyperelastic materials based on the experimental data of [9]. Viscoelastic response is not taken into account in this model as we do not expect it to be important on the short time scales, such as in breast medical applications. Nevertheless, it is possible to incorporate viscoelasticity into our model provided that relevant parameters are available. Boundary conditions in medical applications are usually displacement type which are known relatively accurately. In multimodality imaging which involves X-ray mammography, the boundary conditions are not fully known as the contact surface cannot be identified easily. However, a contact problem formulation as presented in [1] can be used which only requires the magnitude of the compression plate movement.

For breast FE mesh generation, marching-cubes-based techniques such as [10] can be implemented. However, the tetrahedral elements used in these techniques are well known to have unfavorable characteristics, such as slow convergence with mesh refinement. Also, these elements may exhibit overstiffening and volumetric locking especially with incompressible material [11], [12]. Accordingly, with biological soft tissues which are known to be incompressible, using hexahedral elements in the FE model is cost effective and more accurate. To our knowledge, there has been no work done for patient-specific mesh generation of the breast using hexahedral elements. However, computed tomography (CT) has been used by a number of investigators to automate mesh generation in bone. Many investigators [2], [13]–[17] have applied edge-detection algorithms on CT images to generate boundary contours of the struc-

Manuscript received August 9, 2000; revised December 6, 2000. This work was supported by the Terry Fox Foundation under Program Project Grant 006886 and by the U.S. Army under Grant DAMD 17-99-19391. The Associate Editor responsible for coordinating the review of this paper and recommending its publication was M. W. Vannier. Asterisk indicates corresponding author.

\*A. Samani is with the Department of Medical Biophysics, Imaging/Bioengineering Research Group, Sunnybrook and Women's College Health Sciences Centre, University of Toronto, 2075 Bayview Ave., Toronto, ON, M4N 3M5, Canada (e-mail: asamani@sten.sunnybrook.utoronto.ca).

J. Bishop was with the Department of Medical Biophysics, Imaging/Bioengineering Research Group, Sunnybrook and Women's College Health Sciences Centre, University of Toronto, Toronto, ON, M4N 3M5, Canada. He is now with Colorado MEDtec, Inc., Boulder, CO 80301 USA.

M. J. Yaffe and D. B. Plewes are with the Department of Medical Biophysics, Imaging/Bioengineering Research Group, Sunnybrook and Women's College Health Sciences Centre, University of Toronto, Toronto, ON, M4N 3M5, Canada.

Publisher Item Identifier S 0278-0062(01)02773-2.

tures in each image, then employed some techniques to generate the internal mesh. This strategy often requires a significant investment of time by an expert user, and is incapable of automatically generating reasonably accurate meshes for heterogeneous and geometrically complex objects. Other investigators [18]–[20] developed techniques that directly convert image voxels to eight noded hexahedral elements. The resulting object surfaces in these techniques are characterized by abrupt transitions and right angles. As a result, FEM leads to less accurate results, especially on the surface [21], [22]. This paper presents two methods for generating three-dimensional (3-D) meshes of the breast using magnetic resonance imaging (MRI) data. The first method converts image voxels to hexahedral elements and is similar to the said methods except that edge detection is done semi-automatically via segmentation. The second method is based on the transfinite interpolation (TI) technique [23] which is more accurate and efficient in creating smooth surfaces.

To validate the mesh generation component of this model, a cubic agarose phantom with a cylindrical inclusion was constructed and imaged using MRI. Using these images, FE meshes were created using the meshing techniques presented in this paper. To assess the accuracy of these methods, another mesh was created manually based on the known geometry of the phantom. The FEM was applied to these meshes to calculate the deformation and stress distribution resulting from a lateral compression similar to X-ray mammography procedures. The results obtained from both meshes compare well with the manually created mesh results except for the inclusion's circular interface where, as expected, the TI-based mesh produced better results. To demonstrate a potential clinical application of this model, MR images of a healthy volunteer's breast was acquired and a FE mesh was created using the meshing techniques. A lateral compression similar to X-ray mammography procedures was simulated using the TI-based mesh, and calculated MR images are presented in the postcompression configuration.

## II. METHODS

### A. Governing Equations

We use a 3-D FE model to predict breast tissue deformation based on the biomechanical parameters of the breast tissues. While undergoing medical procedures, the breast often deforms significantly. Accordingly, linear elasticity with the infinitesimal deformation formulation is not appropriate to formulate the FE model. As a result, we used a finite deformation formulation in conjunction with hyperelastic material. In a static condition, the equilibrium equation of a body under externally applied forces is

$$\frac{\partial \sigma_{i1}}{\partial x_1} + \frac{\partial \sigma_{i2}}{\partial x_2} + \frac{\partial \sigma_{i3}}{\partial x_3} + f_i = 0; \quad i = 1, 2, 3 \quad (1)$$

where the  $\sigma$ s denote the Cauchy (true) stress tensor components and  $f_i$  represents the body force. In the finite deformation formulation, the current position of a point  $\mathbf{x}$  is obtained by adding the displacement  $\mathbf{u}$  to the corresponding reference position of the same point  $\mathbf{X}$ , i.e.,

$$\mathbf{x} = \mathbf{X} + \mathbf{u}. \quad (2)$$

The stresses are related to displacements ( $\mathbf{u}$ ) via a strain energy function  $U$  which is defined as a function of the strain invariants. These invariants are obtained based on the deformation gradient  $\mathbf{F}$  as follows:

$$\mathbf{F} = \frac{\partial \mathbf{x}}{\partial \mathbf{X}}. \quad (3)$$

To separate the deviatoric and volumetric effects,  $\bar{\mathbf{F}} = J^{-1/3} \mathbf{F}$  is defined, where  $J = \det(\mathbf{F})$  is the third strain invariant which represents the total volume change at the point. Using  $\bar{\mathbf{B}} = \bar{\mathbf{F}} \bar{\mathbf{F}}^T$ , the other strain invariants  $\bar{I}_1, \bar{I}_2$  can be defined as follows:

$$\begin{aligned} \bar{I}_1 &= \text{tr}(\bar{\mathbf{B}}) \\ \bar{I}_2 &= \frac{1}{2} (\bar{I}_1^2 - \text{tr}(\bar{\mathbf{B}} \bar{\mathbf{B}})). \end{aligned}$$

Assuming that a strain energy function  $U = U(\bar{I}_1, \bar{I}_2, J)$  is selected, the true stress tensor can be obtained using the following equation [11]:

$$\boldsymbol{\sigma} = \frac{2}{J} \left[ \left( \frac{\partial U}{\partial \bar{I}_1} + \bar{I}_1 \frac{\partial U}{\partial \bar{I}_2} \right) \bar{\mathbf{B}} - \frac{\partial U}{\partial \bar{I}_2} \bar{\mathbf{B}} \bar{\mathbf{B}} \right] + \frac{\partial U}{\partial J} \mathbf{I} \quad (4)$$

where  $\mathbf{I}$  is the unit matrix. Considering the boundary conditions, (1) and (4) must be solved simultaneously to calculate the displacements  $\mathbf{u}$ . These equations are solved numerically through the FE method. In this method, after the domain is discretized into a number of homogeneous elements, a nonlinear system of equations is formed that is solved iteratively using Newton's method. This formulation is implemented in ABAQUS, a commercial FE software [11]. Discretization, i.e., mesh generation, especially in medical applications, is the most tedious step in a FE analysis. This step is described in the following sections.

### B. Image Acquisition

We have developed meshing techniques which use MR images as an input to create FE meshes. In this work, two sets of MR images were acquired for a phantom and a volunteer's breast. The MR images were acquired using a GE SIGNA 1.5-T scanner (GE Medical Systems, Milwaukee, WI). For the phantom, a 5.0-in surface coil was used to acquire T1-weighted axial images. A two-dimensional (2-D) spin-echo pulse sequence was used with 90° flip angle,  $TR/TE = 400.0/10.5$  msec timing properties,  $12 \times 12$  cm field of view (FOV),  $256 \times 128$  resolution and 1.0-mm slice thickness. A magnitude image of this phantom is shown in Fig. 1, in which the inclusion can be seen with subtle contrast. For the breast, T1 weighted sagittal images were obtained using body coil. A 2-D spin-echo pulse sequence was used with 90° flip angle,  $TR/TE = 300.0/9.0$  ms timing properties,  $20 \times 20$  cm FOV,  $256 \times 128$  resolution, 3.0-mm slice thickness, and three acquisitions.

### C. Image Segmentation and Edge Detection

The purpose of segmentation is to separate different materials within the object of interest. This is done based on the MR signal intensity of different tissues. In the breast, the two main components, i.e., adipose and fibroglandular tissues, must be

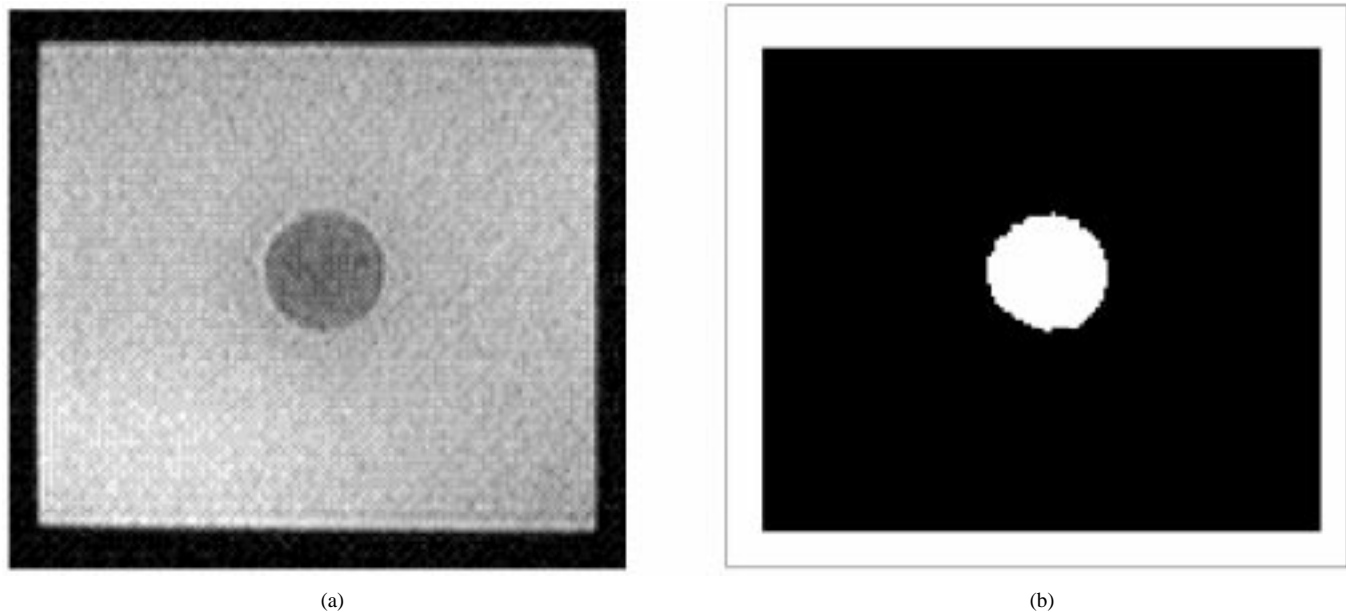


Fig. 1. (a) A typical MR image and (b) a corresponding segmented image of the phantom.

segmented. For edge detection, as the breast tissues have significant signal intensity compared to the background with only noise signal, segmentation results in automatic breast edge detection. For segmentation, 3-D MRI data of the breast is converted into AnalyzeAVW 2.5 [24] database where a standard thresholding-based tool was used to yield segmented images that are suitable for FE mesh generation.

#### D. Voxel-Based (VB) Mesh Generation Technique

Because of the complex geometry of the breast and the structure of the fibroglandular tissue, common mesh generators require a significant amount of user interaction which is very time consuming. As an attempt to minimize user interaction throughout the mesh generation step, we have developed an automatic VB mesh generator with the aim of creating relatively accurate FE meshes of complex volumetric data efficiently. In fact, the only step which requires user interaction in this technique is the segmentation step. To construct the mesh, eight noded hexahedral elements are chosen. This type of element is well known to have many favorable characteristics over tetrahedral elements which can demonstrate overstiffening and locking behavior [12]. Right-angled hexahedrals, however, cannot model curved surface geometries which in turn leads to some inaccuracies in surface strains. To improve the mesh in this respect, we used the smoothing technique of Camacho *et al.* [25] which smooths irregular boundaries at model surfaces and material interfaces.

In the VB methods, since one FE is generated corresponding to each voxel, high resolution MR images may lead to huge FE meshes which, due to current computer power limitations, cannot be processed. Moreover, beyond a certain point, finer FE meshes do not practically improve the solution accuracy. Therefore, reducing image resolution is required to meet computational power constraints. For this purpose, a larger voxel size is selected and using the segmented images, the adipose and fibroglandular tissues voxels within each new voxel are counted.

The new voxel will then be assigned to be as the one with the larger count.

After segmentation and resolution reduction, the mesh generation process is followed by node, and later element generation. For node generation, based on the pixel size, slice thickness and the coordinate system of the MR scanner, the nodes are arranged in the form of a 3-D rectangular lattice which confines the breast volume. The node coordinates of the lattice are calculated and placed in an array. Working with the regular lattice, later, facilitates element generation significantly because each neighbor node can be determined easily and accessed very quickly in the node array. The lattice, however, represents regions both inside and outside the breast. Regions outside the breast are determined during the element generation process and then discarded from the nodes array after element generation is done.

For element generation, the segmented image of each slice is loaded by the computer and stored in a 2-D array. To facilitate finding the boundary of each slice automatically, we assume that the fibroglandular tissue is surrounded by the adipose tissue portion. If this is not the case, a very thin one pixel size layer which represents adipose tissue can be added on the image manually using XV 3.10a image processor [26] to close the boundary where necessary. The boundary points are found by searching the image array line by line first from left to right and then from right to left until an adipose tissue pixel on the left and right boundaries is reached. These points are stored in two arrays that are later used in element generation. Elements corresponding to adipose and fibroglandular tissues are generated in each slice row by row starting from the left boundary point as the local first element node. Other nodes in each element are determined based on the local numbering scheme of hexahedral element. Element generation in a row is continued until the point prior to the right boundary point is reached. This process is repeated for each row to obtain a slice mesh and then for each slice to cover the entire breast. Slice meshes are then stacked to reconstruct a complete 3-D mesh. Skin elements are

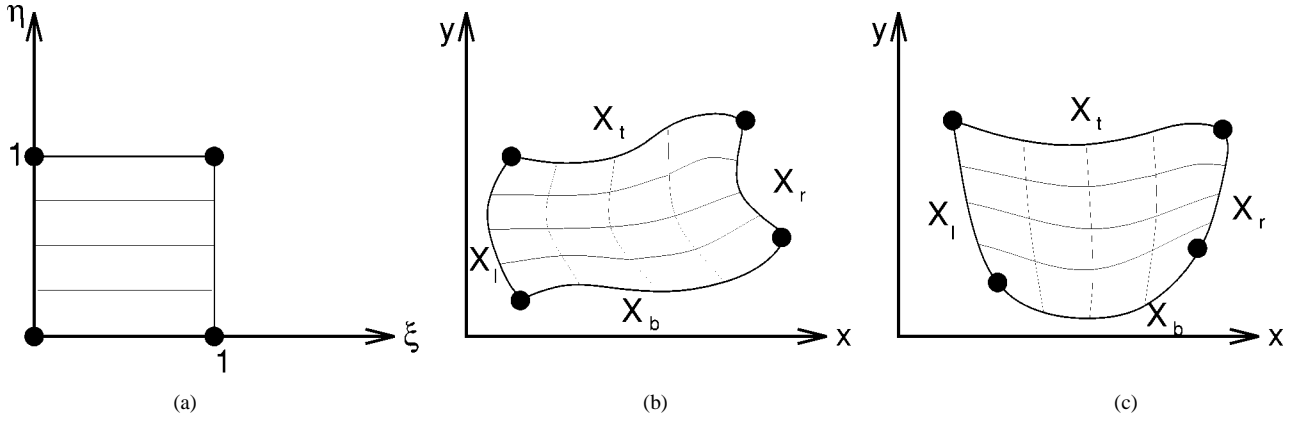


Fig. 2. (a) A unit square (logical space). (b) A typical physical space. (c) Breast boundaries in the TI meshing technique.

generated using four noded quadrilateral membrane elements. These elements are generated by identifying the outer face of elements on the breast surface. Finally, for smoothing, the node coordinates are modified using the smoothing technique of Camacho *et al.* [25]. In this technique, a smoothing coefficient which varies from zero for no smoothing to 0.5 for maximum smoothing, must be selected by the user. While higher factors result in smoother surfaces and interfaces, i.e., better geometry modeling, element distortion caused by this process leads to less accurate FE analysis. Therefore, to achieve optimal results, the smoothing coefficient must be selected or determined carefully. The meshing algorithm is implemented by creating a MATLAB program which inputs the segmented axial, coronal or sagittal images obtained from MRI data, generates the FE mesh, and outputs an input file compatible with ABAQUS FE software [11]. Henceforth, this meshing program will be referred to as VBMESH.

#### E. Transfinite Interpolation Mesh Generation Technique

This technique is based on the idea of mapping a unit square (logical space) to any given shape enclosed by four boundaries (physical space) [23]. To implement this idea in breast FE meshing, after image segmentation, the breast boundary in each slice is divided into three segments. Adding the boundary representing the chest wall, as shown in Fig. 2, the breast area will be enclosed by four boundaries. Although not necessary, these boundaries can be fitted by polynomials to smooth out the surface which is corrupted as a result of segmentation errors. After obtaining the breast boundaries in each slice image, the nodes are generated by mapping the nodes of the unit square grid to a set of nodes distributed inside the boundaries using the following equation:

$$\begin{aligned} X(\xi, \eta) = & (1 - \eta)X_b(\xi) + \eta X_t(\xi) + (1 - \xi)X_l(\eta) \\ & + \xi X_r(\eta) - \xi\eta X_t(1) - \xi(1 - \eta)X_b(1) \\ & - \eta(1 - \xi)X_l(0) - (1 - \xi)(1 - \eta)X_b(0) \end{aligned} \quad (5)$$

where  $\xi$  and  $\eta$  represent the unit square variables and  $X_b$ ,  $X_t$ ,  $X_l$  and  $X_r$  represent the breast's bottom, top, left and right boundaries respectively. Element connections determination in this technique is straight forward as it is done using the nodes of the unit square's grid. Using the same logic, the FE mesh of the skin is created by finding node connections of three of the

unit square's circumferential lines corresponding to the breast's surface. After elements in each slice are generated, as in the previous method, they are stacked to construct a 3-D mesh.

Compared to the VB technique, this method requires a significantly smaller number of elements to represent the true geometry of the breast's surface. Furthermore, this method is capable of locally refining the mesh at an ROI by choosing smaller intervals in the corresponding logical space. Similar to VBMESH, this algorithm was implemented by a MATLAB program which will be, henceforth, referred to as TIMESH.

### III. RESULTS

#### A. Meshing Techniques Validation and Comparison

To validate the meshing techniques, the agarose phantom illustrated in Fig. 3 was constructed. This phantom consists of a block of agar (2%) with a hard cylindrical inclusion made of a mixture of 2% agar and 10% glass beads centered at (32.8, 30.5). The glass beads were used to enhance the contrast in the MR image for segmentation purposes. We assume that the Young's moduli of the block and the inclusion are respectively 11.0 Kpa and 55.0 Kpa. The block is also assumed to undergo a static loading due to 9.0-mm compression resulting from a laterally moving rigid plate toward another stationary plate as illustrated in Fig. 3. The phantom was scanned using a 5.0-in surface coil and a set of 60 MR images was acquired. These images were segmented and the resolution was reduced by a factor of four in the  $x$  and  $y$  directions and to 16 slices in the  $z$  direction. An MR image of the phantom and a corresponding segmented image are shown in Fig. 1. The obtained images were processed by VBMESH using a smoothing coefficient of 0.3 and a FE mesh was created. By dividing the inclusion's circumference into four segments and fitting each segment with a quadratic polynomial, another mesh was created using TIMESH. Finally, based on the known geometry of the phantom, a mesh was created manually as a bench mark. Corresponding to each mesh, an input file compatible with ABAQUS was created. These input files were preprocessed and their corresponding meshes are displayed in Fig. 4. Based on the nonlinear finite deformation FE formulation, the meshes were analyzed using ABAQUS 5.8.1, and as a result, the displacements, strains and stresses were calculated. It is well known that in FE analysis the most significant errors are encountered at material interfaces and curved surfaces which

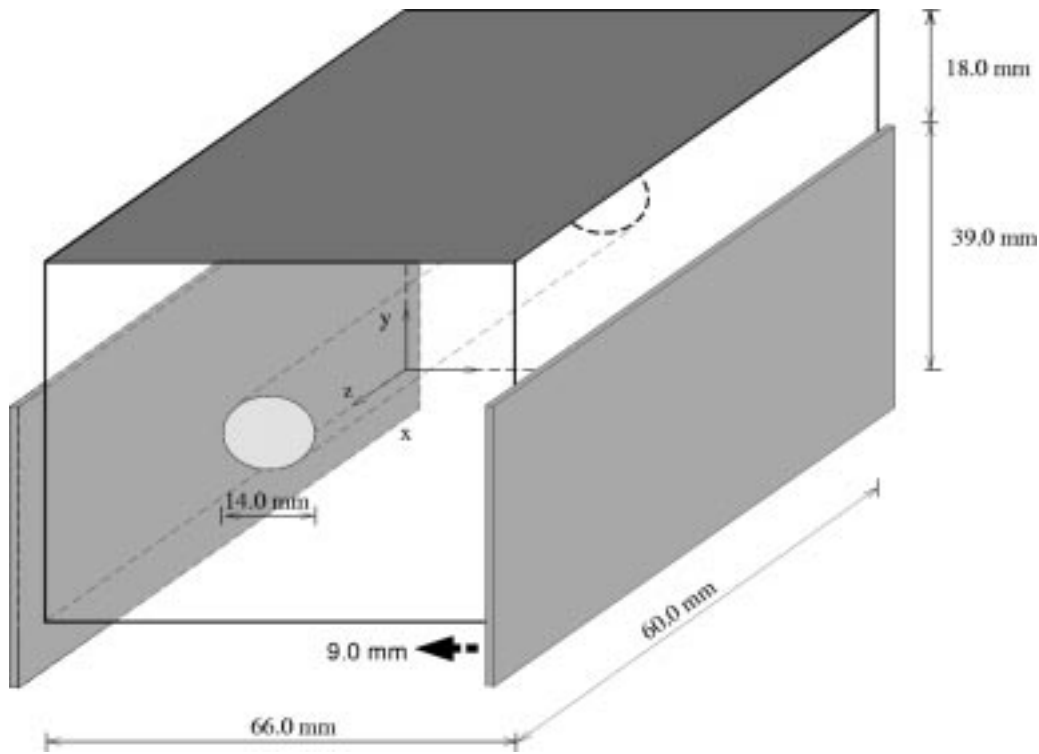


Fig. 3. A schematic of the phantom and its compression model.

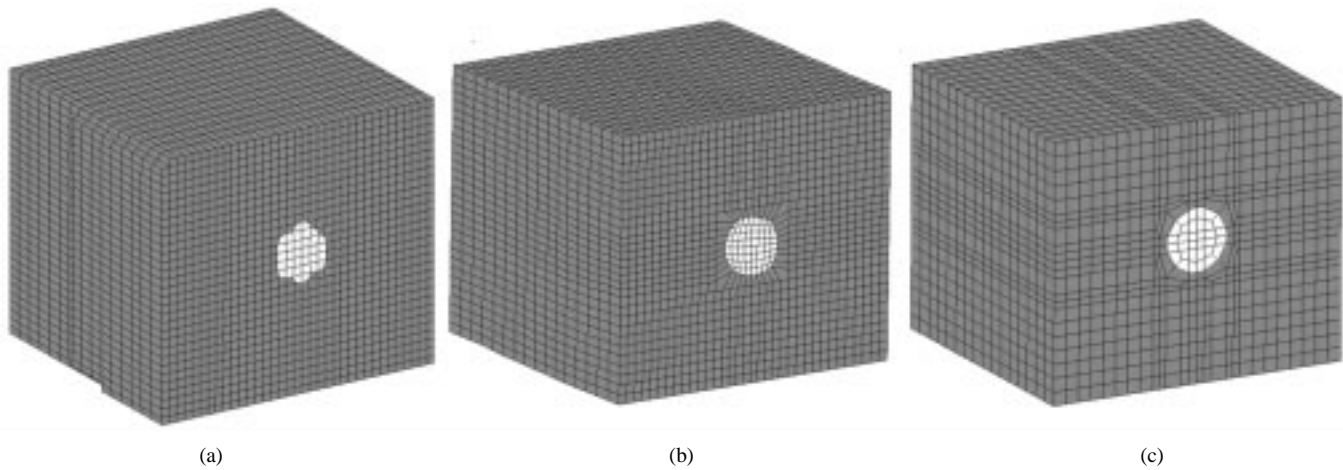


Fig. 4. (a) VB FE mesh, (b) TI-based FE mesh, and (c) A manually created FE mesh of the phantom.

are not represented appropriately by the FE mesh [22]. Therefore, to assess the accuracy of the presented meshing techniques, we will focus on the nodal values at the inclusion's circumference. As an example, the results of a displacement, a strain, and a stress component at this region in the middle plane are displayed in Fig. 5, which qualitatively indicates the better performance of the TI-based technique. To make a quantitative comparison, the average  $\bar{E}$  and standard deviation  $\sigma$  of the relative error of the displacement, strain and stress over the inclusion's circumferential nodes are calculated and summarized in Table I. The results clearly indicate that the TI-based technique leads to more accurate FE meshes. Moreover, compared to the displacements errors, the strain and stress errors are significantly larger. This can be justified based on the fact that calculating

both strains and stresses involves calculating the derivatives of displacements which leads to error magnification.

### B. Breast Image Nonrigid Registration

To examine our model in a complex clinical problem, we applied it to a breast image registration problem where the breast was compressed by two plates causing nonrigid deformation. For this purpose, sagittal MR images of a breast of a healthy volunteer were acquired at 6-mm intervals at a resolution of 0.625 mm/pixel. These images were segmented with AnalyzeAVW 2.5 and the resulting images were processed to create FE meshes. A typical sagittal MR image of the breast and a corresponding segmented image are shown in Fig. 6(a) and (b). The objective here was to calculate MR images of

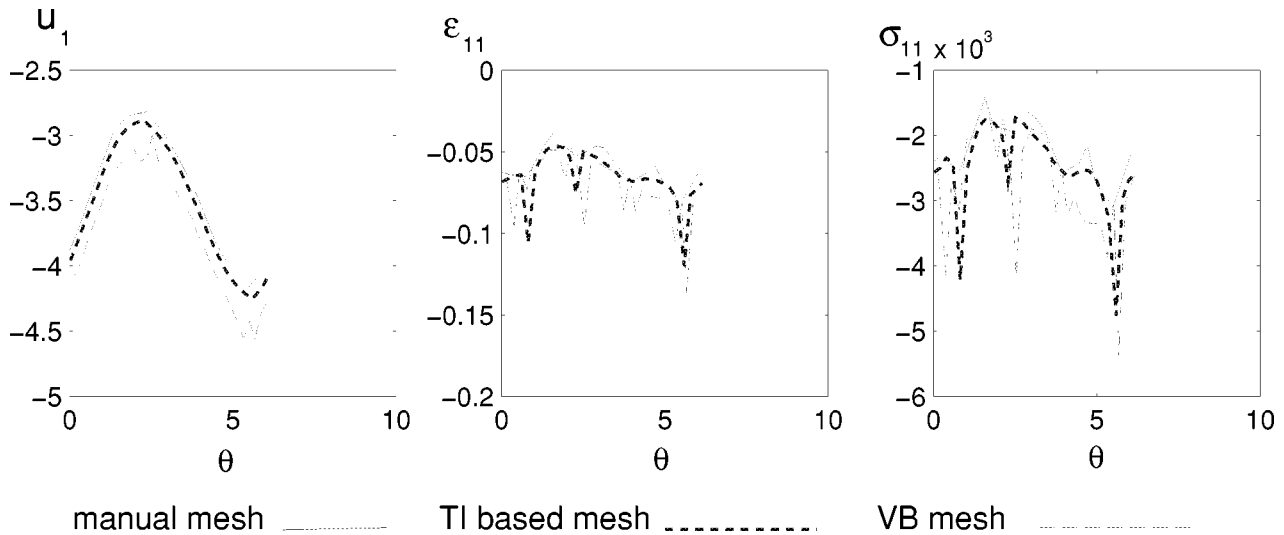


Fig. 5. Variations of the displacement, normal strain, and normal stress in the compression direction around the inclusion's circumference.

TABLE I  
AVERAGE RELATIVE ERRORS  $\bar{E}$  AND STANDARD DEVIATION  $\sigma$  OF  
DISPLACEMENTS, STRAINS, AND STRESSES OF THE CALCULATED MESHES AT  
THE INCLUSION'S SURFACE

| Displacements          | $u_1$           | $u_2$           | $u_3$           | -               | -               | -               |
|------------------------|-----------------|-----------------|-----------------|-----------------|-----------------|-----------------|
| VB Mesh: $\bar{E}$ (%) | 7.50            | 7.93            | 5.67            | -               | -               | -               |
| $\sigma$ (%)           | 1.38            | 4.07            | 3.07            | -               | -               | -               |
| TI Mesh: $\bar{E}$ (%) | 1.70            | 2.04            | 0.84            | -               | -               | -               |
| $\sigma$ (%)           | 0.50            | 1.69            | 0.78            | -               | -               | -               |
| Strains                | $\epsilon_{11}$ | $\epsilon_{22}$ | $\epsilon_{33}$ | $\epsilon_{12}$ | $\epsilon_{13}$ | $\epsilon_{23}$ |
| VB Mesh: $\bar{E}$ (%) | 18.14           | 16.94           | 6.32            | 16.56           | 20.86           | 20.89           |
| $\sigma$ (%)           | 7.00            | 9.79            | 4.79            | 11.00           | 15.23           | 20.91           |
| TI Mesh: $\bar{E}$ (%) | 14.24           | 8.08            | 9.82            | 17.89           | 13.10           | 16.33           |
| $\sigma$ (%)           | 11.25           | 7.17            | 2.83            | 12.83           | 10.21           | 17.27           |
| Stresses               | $\sigma_{11}$   | $\sigma_{22}$   | $\sigma_{33}$   | $\sigma_{12}$   | $\sigma_{13}$   | $\sigma_{23}$   |
| VB Mesh: $\bar{E}$ (%) | 17.15           | 14.55           | 9.37            | 16.56           | 20.86           | 20.89           |
| $\sigma$ (%)           | 9.32            | 14.89           | 10.32           | 11.00           | 15.23           | 20.91           |
| TI Mesh: $\bar{E}$ (%) | 13.20           | 8.21            | 12.03           | 17.89           | 13.10           | 16.33           |
| $\sigma$ (%)           | 10.70           | 8.31            | 5.36            | 12.83           | 10.21           | 17.27           |

this breast as if it underwent 8.0-mm compression. For this purpose, two FE meshes were first created using the VB and TI-based techniques. After image segmentation and resolution reduction by a factor of 4 in each direction, the resulting images were processed by VBMesh using a smoothing coefficient of 0.3. The resulting mesh consists of 16 841 elements and 15 939 nodes and is characterized by an abrupt surface. Using the segmented images, the TI-based mesh was created using TIMESH. This mesh was calculated by fitting a third-order polynomial to the boundary representing the chest wall while fitting quadratic polynomials to the breast surface's three segments. The resulting mesh consists of 2280 elements and 2059 nodes and, unlike the VB mesh, has a smooth surface. The FE meshes of one slice created using the VB and the TI-based techniques are depicted in Fig. 6(c) and (d). Fig. 7 depicts the VB mesh, the TI-based mesh of the entire breast, and the breast FE model undergoing compression. The adipose and fibroglandular tissues were assumed to be incompressible and hyperelastic, and the corresponding parameters were obtained by fitting experimental data [9] to a hyperelastic Neo-Hookean model. For this purpose, the data represented as Young's

modulus versus strain were converted to stress versus strain by first fitting quadratic and third-order polynomials to the adipose and fibroglandular tissues data, respectively, then integrating over the strain. The resulting fitting polynomials of the Young's modulus versus strain of the adipose and fibroglandular tissues are as follows:

$$E = 0.5197\epsilon^2 + 0.0024\epsilon + 0.0049; \quad \text{for fat}$$

$$E = 123.8889\epsilon^3 - 11.7667\epsilon^2 + 0.6969\epsilon + 0.0121; \quad \text{for parenchyma.}$$

To the authors' knowledge, the experimental data [9] are the only available breast tissue hyperelastic properties data obtained based on the large deformation theory considerations. Nevertheless, as the standard deviation of this data is high, more accurate and reliable data is required to produce better image registration results. Skin, in general, is well known to be anisotropic and hyperelastic [27]. However, it can be approximated by an isotropic and linear elastic model provided that the strain does not exceed 50% [27], [28]. Accordingly, as the skin strain in this application is expected to be well below 50%, it was assumed to be elastic with a Young's modulus of 10.0 kPa [28] and a thickness of 1.0 mm. The chest wall was assumed to provide zero displacement boundary conditions while the specified displacement or force boundary conditions on the breast's surface is not known because the contact surface between the breast and the plates increases over the course of compression. Accordingly, this problem was formulated as a 3-D contact problem and ABAQUS' contact solver with the finite deformation theory formulation was used. This highly nonlinear problem was solved iteratively and, as a result, the breast tissue displacements were calculated. These displacements, in combination with the MR images of the uncompressed breast, were used to obtain simulated MR images of the compressed breast. A number of consecutive sagittal MR images of the breast before compression, along with their corresponding simulated images after compression, are depicted in Fig. 8. In this figure, reasonable translation and tissue expansion can be observed by comparing the two sets of images. For example, image (g') from the simulated set and

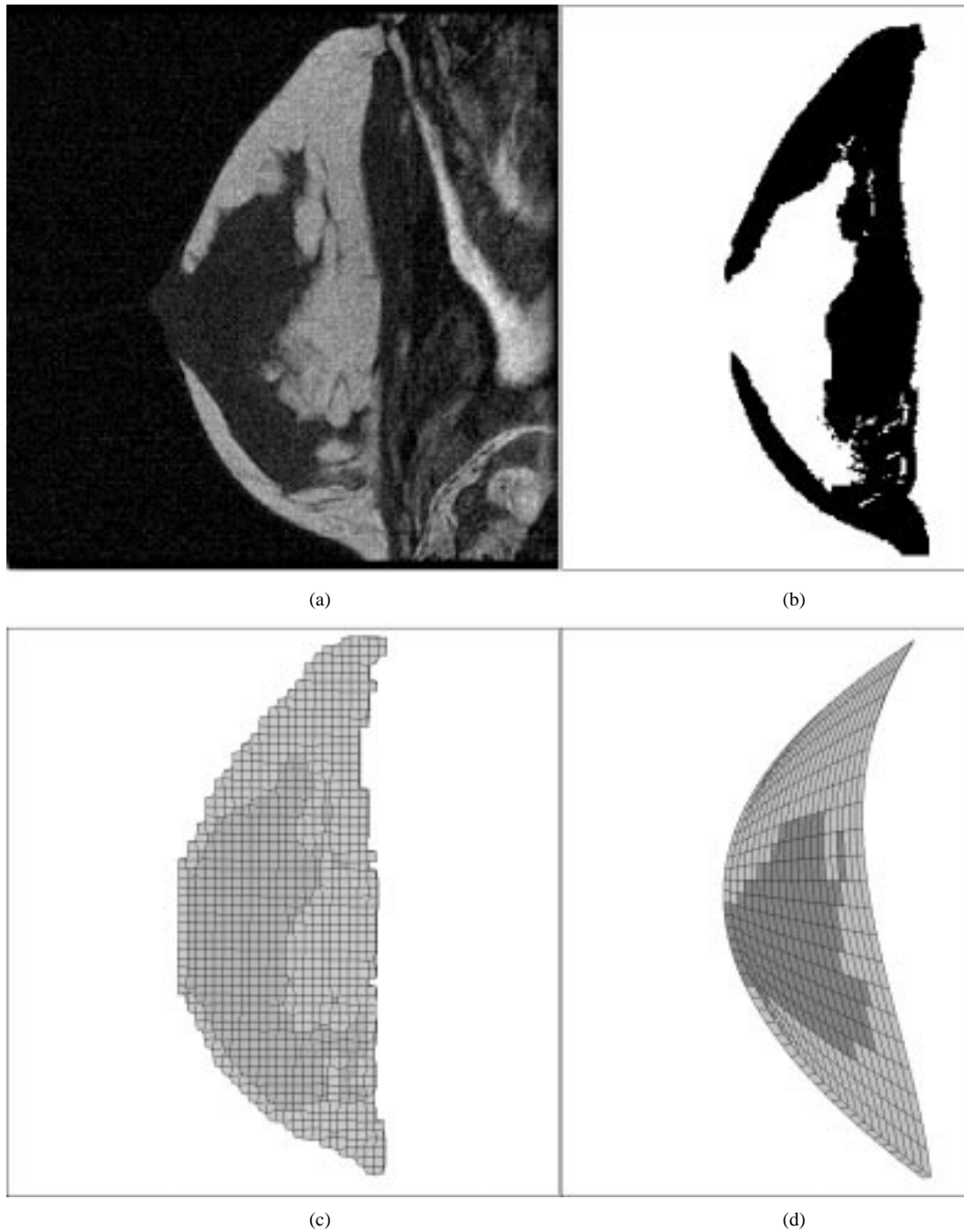


Fig. 6. (a) A MR image and (b) a corresponding segmented image, (c) VB FE mesh, and (d) TI-based FE mesh of one breast slice.

image (f) from the MR image set, which approximately correspond to the same slice, depict similar anatomical features. The same can be observed in other image pairs such as  $(a, b')$ ,  $(b, c')$ , etc.

#### IV. DISCUSSION

We have presented a FE model, based on biomechanical principles, to predict breast tissue deformations. This model can serve as a guideline in numerous clinical applications, such as breast image registration, multimodality data fusion, breast surgery, and biopsy. The first component of this model is FE

meshing, for which two meshing techniques were presented and evaluated. These techniques, which require minimal user interaction, use MRI images of the breast to produce patient-specific FE meshes. Using a numerical experiment, the TI-based meshing technique, which requires fewer elements to represent the geometry of curved surfaces relatively accurately, proved to generate more accurate displacements and stresses. Moreover, unlike the VB technique, this technique is capable of refining the mesh at an arbitrary ROI. The adipose and fibroglandular tissues are modeled as incompressible and hyperelastic materials while the skin is modeled using membrane elements with linear elastic properties. These tissues are assumed to

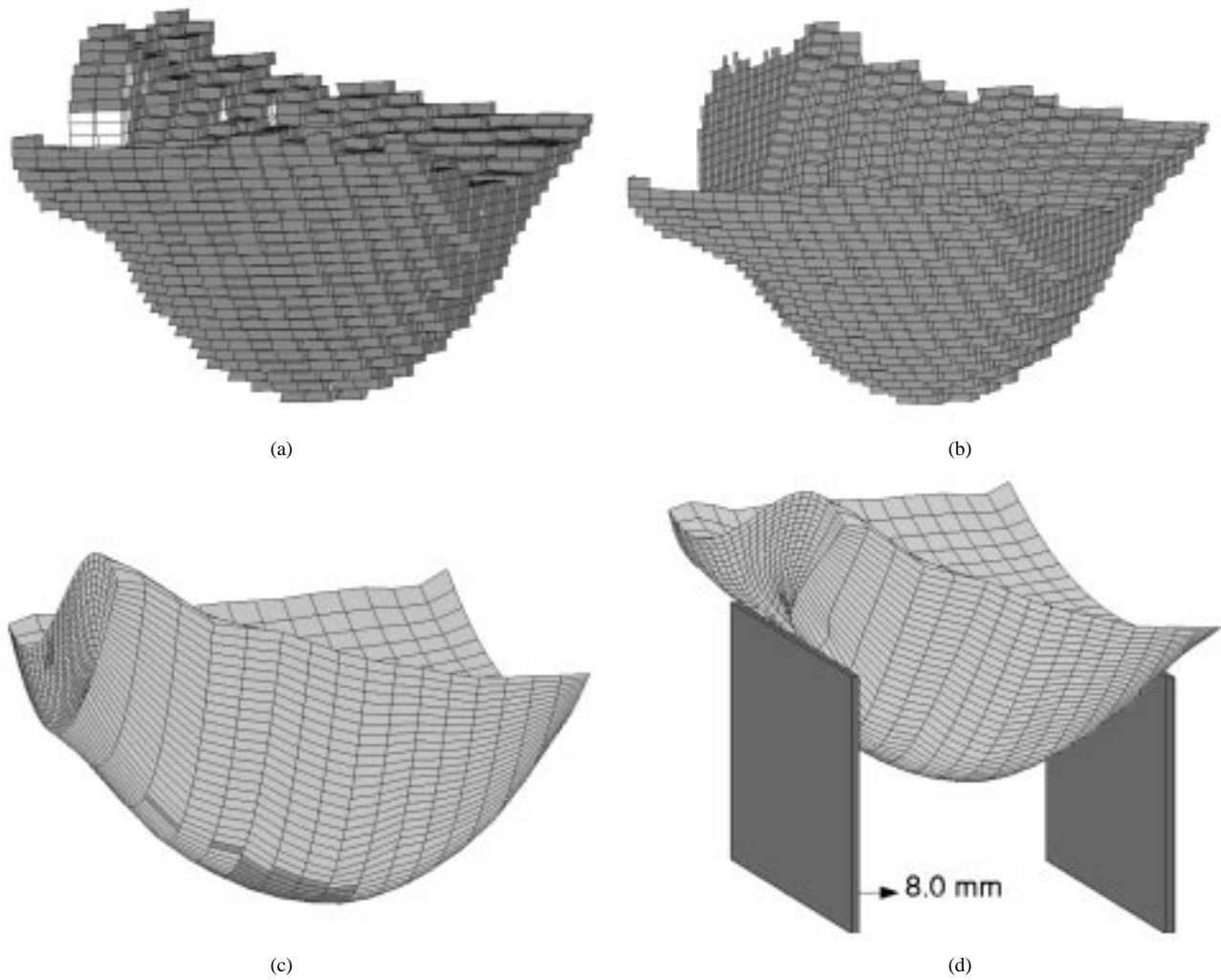


Fig. 7. (a) VB 3-D FE mesh of the breast slice excluding the skin, (b) corresponding skin mesh, (c) TI-based FE mesh of the breast, and (d) the deformed shape of the breast under compression.

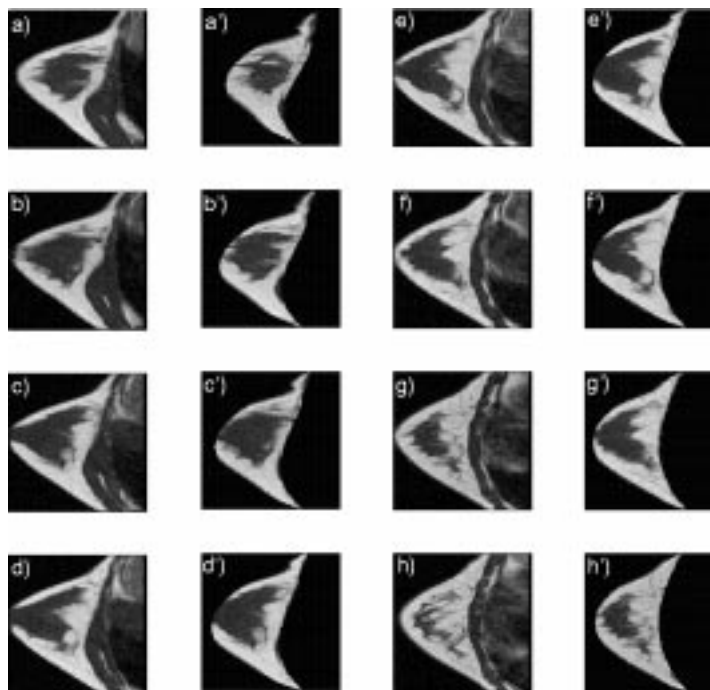


Fig. 8. MR images of the breast before compression (*a*, *b*, *c*, etc.) and simulated images of the compressed breast (*a'*, *b'*, *c'*, etc.).



undergo large deformations. As for boundary conditions, the chest wall region is assumed to provide zero displacements boundary conditions while the specified boundary conditions depend on the clinical application. For example, in the breast image registration problem, as was previously presented, this boundary condition type is not known explicitly and the problem is formulated as a 3-D contact problem. An image registration example was presented to evaluate the FE model's effectiveness in complex clinical applications. The results summarized in Fig. 8 qualitatively prove the merits of this model. Quantitative validation, however, is beyond the scope of this paper as it requires more reliable breast tissue hyperelastic properties data. Research is underway in our laboratory to acquire such data which will pave the way for conducting this validation.

## REFERENCES

- [1] A. Samani, J. Bishop, E. Ramsay, and D. Plewes, "Breast tissue deformation finite element modeling for MRI/X-ray mammography data fusion," presented at the 5th Int. Workshop Digital Mammography, Toronto, ON, Canada, 2000.
- [2] J. H. Keyak, J. M. Meagher, H. B. Skinner, and C. D. Mote, "Automated three-dimensional finite element modeling of bone: A new method," *J. Biomed. Eng.*, vol. 12, pp. 389–397, 1990.
- [3] R. Müller and P. Rüeggsegger, "Three-dimensional finite element modeling of noninvasively assessed trabecular bone structure," *Med. Eng. Phys.*, vol. 17, no. 2, pp. 126–133, 1995.
- [4] W. Krach, T. J. Rammerstorfer, T. J. Reiter, and P. Zenz, "In vivo CT-based 3-D-modeling of human bones with respect to inhomogeneity," in *Proc. ASME Bioengineering Conf.*, vol. BED-29, 1995, pp. 57–58.
- [5] J. M. Guccione, K. D. Costa, and A. D. McCulloch, "Finite element stress analysis of left ventricular mechanics in the beating dog heart," *J. Biomech.*, vol. 28, pp. 1167–1177, 1995.
- [6] S. K. Kyriacou, C. Davatzikos, S. J. Zinreich, and R. N. Bryan, "Non-linear elastic registration of brain images with tumor pathology using a biomechanical model," *IEEE Trans. Med. Imag.*, vol. 18, pp. 580–592, July 1999.
- [7] M. I. Miga, J. M., K. D. Paulsen, Lemery, S. D. Eisner, A. Hartov, F. E. Kennedy, and W. R. D., "Model-updated image guidance: Initial clinical experiences with gravity-induced brain deformation," *IEEE Trans. Med. Imag.*, vol. 18, pp. 866–874, Oct. 1999.
- [8] A. Hagemann, K. Rohr, H. S. Stiehl, U. Spetzger, and J. M. Gilsbach, "Biomechanical modeling of the human head for physically based non-rigid image registration," *IEEE Trans. Med. Imag.*, vol. 18, pp. 875–884, Oct. 1999.
- [9] P. S. Wellman, "Tactile imaging," Ph.D. dissertation, Harvard Univ., Cambridge, MA, 1999.
- [10] J. M. Sullivan Jr., G. Charron, and K. D. Paulsen, "A three-dimensional mesh generator for arbitrary multiple material domain," *Finite Elements Anal. Design*, vol. 25, pp. 219–241, 1997.
- [11] *ABAQUS, Theory Manual*, Hibbit, Karlsson, and Sorenson, Pawtucket, RI, June 1998.
- [12] T. J. R. Hughes, *The Finite Element Method, Linear Static and Dynamic Finite Element Analysis*. Englewood Cliffs, NJ: Prentice-Hall, 1987.
- [13] R. T. Hart, V. V. Hennebel, N. Thongpreda, W. C. Van Buskirk, and R. C. Anderson, "Modeling the biomechanics of the mandible: A three-dimensional finite element study," *J. Biomech.*, vol. 25, pp. 261–286, 1992.
- [14] M. J. Rudert and T. D. Brown, "Toward automation of finite element models for bone grafting of femoral head osteonecrosis," in *Proc. ASME Bioengineering Conf.*, vol. BED-28, 1994, pp. 145–146.
- [15] V. K. Goel, H. Park, and W. Kong, "Investigation of vibration characteristics of the ligamentous spine using the finite element approach," *J. Biomech. Eng.*, vol. 116, pp. 377–383, 1994.
- [16] E. H. II Moor, D. A. Schauer, and J. A. Weiss, "Mesh generation for a finite element model of the human leg," in *Proc. ASME Bioengineering Conf.*, vol. BED-29, 1995, pp. 51–52.
- [17] L. Voo, J. A. Denman, N. Yoganandan, and F. Pintar, "A 3-D model of the cervical spine with ct-based geometry," *Adv. Bioeng.*, vol. 29, pp. 323–324, 1995.
- [18] D. P. Fyhrie, M. S. Hamid, R. F. Kuo, and S. M. Lang, "Direct three-dimensional finite element analysis of human vertebral cancellous bone," in *Proc. 38th Annu. Meeting Orthopedic Research Society*, vol. 17, 1992, p. 551.
- [19] S. J. Hollister and N. Kikuchi, "Direct analysis of trabecular bone stiffness and tissue level mechanics using an element by element homogenization method," in *Proc. 38th Annu. Meeting Orthopedic Research Society*, vol. 17, 1992, p. 559.
- [20] B. van Rietbergen, H. Weinans, R. Huiskes, and A. Odgaard, "A new method to determine trabecular bone elastic properties and loading using micromechanical finite-element models," *J. Biomech.*, vol. 28, pp. 69–81, 1995.
- [21] C. R. Jacobs, J. A. Mandell, and G. S. Beaupre, "A comparative study of automatic finite element mesh generation techniques in orthopedic biomechanics," in *Proc. ASME Bioengineering Conf.*, vol. BED-24, 1993, pp. 512–514.
- [22] R. E. Guldberg and S. J. Hollister, "The accuracy of digital image-based finite element models," *J. Biomech. Eng.*, vol. 120, no. 2, pp. 289–295, 1998.
- [23] P. Knupp and S. Steinberg, *Fundamentals of Grid Generation*. Boca Raton, FL: CRC, 1994.
- [24] "AnalyzeAVW, Ver. 2.5," Mayo-Foundation, Rochester, MN, 1998.
- [25] D. L. A. Camacho, R. H. Hopper, G. M. Lin, and B. S. Myers, "An improved method for finite element mesh generation of geometrically complex structures with application to the skullbase," *Biomechanics*, vol. 30, no. 10, pp. 1067–1070, 1997.
- [26] *XV, Ver. 3.10a*, J. Bradley, 1994.
- [27] P. Tong and Y. C. Fung, "The stress-strain relationship for the skin," *J. Biomechanics*, vol. 9, pp. 649–657, 1976.
- [28] J. E. Bischoff, E. M. Arruda, and K. Grosh, "Finite element modeling of human skin using an isotropic, nonlinear elastic constitutive model," *J. Biomech.*, vol. 33, pp. 645–652, 2000.